

# Investigation of 1:1 resonance in a rotating 4<sup>th</sup> degree and order gravitational field

Jinglang Feng<sup>1)</sup>, Ron Noomen<sup>2)</sup>, Xiyun Hou<sup>1)</sup>, Pieter Visser<sup>2)</sup>,  
Jianping Yuan<sup>3)</sup>, Jingshi Tang<sup>1)</sup>, Lin Liu<sup>1)</sup>

<sup>1)</sup>Nanjing University, China; <sup>2)</sup>Delft University of Technology, the Netherlands;

<sup>3)</sup>Northwestern Polytechnic University, China.

Applying a gravitational field truncated at the 4<sup>th</sup> degree and order, the 1:1 ground-track resonance is investigated. To address the main properties of this 1:1 resonance, a 1-degree of freedom (1-DOF) system is studied firstly. Its equilibrium points (EPs), stability and resonance width are obtained. Different from previous studies, the inclusion of non-spherical terms higher than degree and order 2 introduces new phenomena. For a further study about the 1:1 resonance, a 2-DOF system is introduced, which includes the 1-DOF system and a second resonance playing a perturbation role. With the aid of Poincaré sections, the generation of chaos in the phase space is studied in detail by addressing the overlap process of these two resonances with arbitrary combinations of eccentricity ( $e$ ) and inclination ( $i$ ). The situations of complete chaos are estimated in the  $e - i$  plane. By applying the maximum Lyapunov Characteristic Exponent (LCE), chaos is characterized quantitatively and similar conclusions can be achieved. This study is applied to asteroid 1996 HW1.

**Keyword :** Asteroid, Resonance, Stability, Chaos

## 1. Introduction

The commensurability (usually a ratio of simple integers) between the rotation of the primary body and the orbital motion of the surrounding spacecraft or particle is called ground-track resonance. A large amount of research has been carried out about geosynchronous orbits. For example, a 2-DOF Hamiltonian system was modeled<sup>1)</sup> near the critical inclination perturbed by the inhomogeneous geopotential. Global dynamics were studied in terms of Poincaré maps in the plane of inclination and argument of pericenter. Chaotic motions were expected close to the separatrix of the resonance of the mean motion.

However, for ground-track resonances in a highly irregular gravitational field (mainly small solar system bodies), studies are limited. Scheeres<sup>2)</sup> studied the stability of the 1:1 mean motion resonance with a rotating asteroid using a triaxial ellipsoid model, and applied it to Vesta, Eros and Ida. Later on, he studied the effect of the resonance between the rotation rate of asteroid Castalia and the true anomaly rate of an orbiting particle at periapsis with a 2<sup>nd</sup> degree and order gravitational field<sup>3)</sup>. This kind of resonance was proven to be responsible for significant changes of orbital energy and eccentricity, and provides a mechanism for an ejected particle to transfer into a hyperbolic orbit or vice versa. By considering the 2<sup>nd</sup> degree and order gravitational field, Hu and Scheeres<sup>4)</sup> showed that orbital resonance plays a significant role in determining the stability of orbits. Further, by modelling the resonant dynamics in a uniformly rotating 2<sup>nd</sup> degree and order gravitational field as a 1-DOF pendulum Hamiltonian<sup>5)</sup>, widths of the resonance were obtained in analytical expressions and also tested against numerical simulations for five resonances. They were found to be independent of the rotation rate and mass of the central body but strongly dependent on  $e$  and  $i$ . The retrograde orbits have a smaller resonance region than the prograde ones. In a

slowly rotating gravitational field, the orbital stability was explained by the distance between the resonances but not by the strength of a specific one using the overlap criteria.

The resonant structure can be explained with the truncated model for the equatorial and circular cases, respectively. Delsate<sup>6)</sup> built the 1-DOF Hamiltonian of the ground-track resonances of Dawn orbiting Vesta. The locations of the EPs and the resonance width were obtained for several main resonances (1:1, 1:2, 2:3 and 3:2). The results were checked against numerical tests. The 1:1 and 2:3 resonances were found to be the largest and strongest ones, respectively. The probability of capture in the 1:1 resonance and escape from it was found to rely on the resonant angle. Tzirti and Varvoglis<sup>7)</sup> extended Delsate's work by introducing  $C_{30}$  into the 1:1 resonance, which resulted in 2-DOF dynamics. The  $C_{30}$  term was found to create tiny chaotic layers around the separatrix but without significant influence on the resonance width. With the ellipsoid shape model<sup>8)</sup>, MEGNO (Mean Exponential Growth factor of Nearby Orbits) was applied as an indicator to detect stable resonant periodic orbits and also 1:1 and 2:1 resonance structures under different combinations of the three semi-axes of the ellipsoid. A 1-DOF resonant model parametrized by  $e$  and  $i$  was obtained with a truncated ellipsoidal potential up to degree and order 2.

For the previous studies, the limitations are either the gravitational field which is truncated at degree and order 2 or the orbit which is restricted to a circular or polar case. In this study, the harmonic coefficients up to degree and order 4 are taken into account for studying the 1:1 resonance at different combinations of  $e$  and  $i$ , which results in a 2-DOF model. Therefore, this paper is arranged as follows. Firstly, a 1-DOF Hamiltonian is built to investigate the main properties of the 1:1 resonance. The location of EPs and their stability are solved numerically for different combinations of  $e$  and  $i$  for 1996 HW1. The resonance widths of the stable EPs are found numerically. Secondly, a 2-DOF Hamiltonian is introduced

with the inclusion of a second resonance, which is treated as a perturbation on the 1-DOF Hamiltonian. Chaos is generated due to the overlap of the two resonances. By applying Poincaré sections, the extent of the chaotic region in the phase space is examined against the distance between the primary and second resonances and their respective strengths. The roles that  $e$  and  $i$  play in the evolution of chaos in the phase space are studied systematically. Finally, the maximal LCE (mLCE) of the orbits in the chaotic seas are calculated for a quantitative study.

## 2. Dynamical Modelling

### 2.1. Hamiltonian of the system

The gravity potential expressed in orbital elements  $(a, e, i, \Omega, \omega, M)$  is given by Kaula<sup>9)</sup> as

$$V = \frac{\mu}{r} + \sum_{n \geq 2} \sum_{m=0}^n \sum_{p=0}^n \sum_{q=-\infty}^{\infty} \frac{\mu R_e^n}{a^{n+1}} F_{nmp}(i) G_{npq}(e) S_{nmpq}(\omega, M, \Omega, \theta) \quad (1)$$

in which  $\mu$  and  $R_e$  are the gravitational constant and reference radius of the body, respectively.  $r$  is the distance between the point of interest and the center of mass of the body.  $F(i)$  and  $G(e)$  are functions of inclination and eccentricity, respectively. The complete list of them up to degree and order 4 can be found in Kaula<sup>9)</sup>. In addition,  $n, m, p, q$  are all integers, and  $\theta$  is the sidereal angle.

$$S_{nmpq} = \begin{bmatrix} C_{nm} \\ -S_{nm} \end{bmatrix}_{n-m \text{ odd}}^{n-m \text{ even}} \cos \Theta_{nmpq} + \begin{bmatrix} S_{nm} \\ C_{nm} \end{bmatrix}_{n-m \text{ odd}}^{n-m \text{ even}} \sin \Theta_{nmpq}$$

with Kaula's phase angle  $\Theta_{nmpq}$  written as

$$\Theta_{nmpq} = (n-2p)\omega + (n-2p+q)M + m(\Omega - \theta)$$

Given the Delaunay variables

$$l = M, g = \omega, h = \Omega$$

$$L = \sqrt{\mu a}, G = L\sqrt{1-e^2}, H = G \cos i$$

the Hamiltonian of the system can be written as

$$\mathcal{H} = T - V + \dot{\theta}\Lambda \quad (2)$$

in which  $T = -\mu^2/2L^2$  is the kinetic energy,  $\dot{\theta}$  is the rotation rate of the asteroid and  $\Lambda$  is the momentum conjugated to  $\theta$ . Resonances occur when the time derivative  $\dot{\Theta}_{nmpq} \approx 0$ . The 1:1 resonance is studied in detail in the following sections.

### 2.2. 1:1 Resonance

According to Ref. 9), to study the 1:1 resonance, the resonant angle is introduced and defined as  $\sigma = \lambda - \theta$ , with the mean longitude  $\lambda = \omega + M + \Omega$ . This resonance occurs at  $\dot{\sigma} \approx 0$ , which means that the revolution rate (mean motion) of the orbit is commensurate with the rotation rate of the asteroid. In addition, it should be noticed that the solution of this 1:1 resonance includes the equilibrium points (EPs) that are commonly studied in a rotating (or body-fixed) frame, and  $\sigma$  is the phase angle of the EPs in a rotating frame.

The spherical harmonics up to degree and order 4 that contribute to this resonance are listed in Appendix A. To introduce the resonant angle  $\sigma$  in the Hamiltonian and also keep the new variables canonical, a symplectic transformation is applied

$$d\sigma \cdot L' + d\theta' \cdot \Lambda' = d\lambda \cdot L + d\theta \cdot \Lambda$$

and a new set of canonical variables is obtained as

$$\sigma, L' = L, \theta' = \theta, \Lambda' = \Lambda + L$$

After averaging over the fast variable  $\theta'$ , the Hamiltonian for the 1:1 resonance truncated at the second order of  $e$  can be written as

$$\mathcal{H} = \mathcal{H}_0 + \mathcal{H}_1 + \mathcal{H}_2 + o(e^3)$$

where  $\mathcal{H}_k$  ( $k = 1, 2$ ) is the Hamiltonian at the  $k^{\text{th}}$  order of  $e$  and  $\mathcal{H}_0$  is expressed as

$$\begin{aligned} \mathcal{H}_0 = & -\frac{\mu^2}{2L^2} + \dot{\theta}(\Lambda' - L) - \frac{\mu^4 R^2}{L^6} [C_{20}(1-e^2)^{\binom{-3}{2}} \left(-\frac{1}{2} + \frac{3s^2}{4}\right) \\ & + \frac{3}{4} \left(1 - \frac{5e^2}{2} + \frac{13e^4}{16}\right) (1+c)^2 (C_{22} \cos(2\sigma) + S_{22} \sin(2\sigma))] \\ & - \frac{\mu^5 R^3}{L^8} \left[ \left(1 + 2e^2 + \frac{239e^4}{64}\right) \left(-\frac{3}{4}(1+c) + \frac{15}{16}(1+3c)s^2\right) \right. \\ & \left. (C_{31} \cos \sigma + S_{31} \sin \sigma) + \frac{15}{8} \left(1 - 6e^2 + \frac{423e^4}{64}\right) (1+c)^3 \right. \\ & \left. (C_{33} \cos(3\sigma) + S_{33} \sin(3\sigma)) \right] - \frac{\mu^6 R^4}{L^{10}} [C_{40}(1-e^2)^{\binom{-7}{2}} \\ & \left. \left(\frac{3}{8} - \frac{15s^2}{8} + \frac{105s^4}{64}\right) + \left(1 + e^2 + \frac{65e^4}{16}\right) \right. \\ & \left. \left(-\frac{15}{8}(1+c)^2 + \frac{105}{8}(c+c^2)s^2\right) (C_{42} \cos(2\sigma) + S_{42} \sin(2\sigma)) \right. \\ & \left. + \frac{105}{16} \left(1 - 11e^2 + \frac{199e^4}{8}\right) (1+c)^4 (C_{44} \cos(4\sigma) + S_{44} \sin(4\sigma)) \right] \end{aligned} \quad (3)$$

in which  $c = \cos(i)$ ,  $s = \sin(i)$  and  $L$  is used hereafter instead of  $L'$  for convenience. In terms of angular variables, it can be seen that  $\mathcal{H}_0$  is only dependent on the angle  $\sigma$ . Since  $\theta'$  is implicit in  $\mathcal{H}_0$ , its conjugate  $\Lambda'$  is a constant and can be dropped. Similarly,  $G$  and  $H$ , which are related to  $e$  and  $i$ , are constant as  $g$  and  $h$  are absent in  $\mathcal{H}_0$ . Therefore at a given combination of  $e$  and  $i$ ,  $\mathcal{H}_0$  is actually a 1-DOF system. However,  $\mathcal{H}_1$  and  $\mathcal{H}_2$  are functions of both  $\sigma$  and  $g$  and include angles  $j\sigma + kg$  ( $j = 1, 2, 3, k = \pm 1, \pm 2$ ), and therefore are 2-DOF systems. Their expressions are given in Appendix A and they are both zero at  $e = 0$  or  $i = 0$ .

According to our simulations, it is found that  $\mathcal{H}_1 \in \mathcal{O}(\epsilon^{3/2})$ ,  $\mathcal{H}_2 \in \mathcal{O}(\epsilon)$ , where  $\epsilon$  is the ordering parameter which ranges from  $10^{-2}$  to  $10^{-1}$ . Since the origin of our selected body-fixed frame is located at the center mass of the asteroid and the axes are aligned with the principal moments of inertia of the asteroid, the  $C_{21}$ ,  $S_{21}$  and  $S_{22}$  terms are all zero, leading to the fact that the magnitude of  $\mathcal{H}_1$  is smaller than that of  $\mathcal{H}_2$ . Therefore,  $\mathcal{H}_0$  with resonant angle  $\sigma$  can be viewed as being responsible for the primary resonance.  $\mathcal{H}_1$  and  $\mathcal{H}_2$  are the cause of the second resonances, which are

expected to give rise to chaos.

### 3 Primary Resonance

#### 3.1. EPs and Resonance Width

Firstly,  $\mathcal{H}_0$  is studied in detail. Its equilibria can be found by numerically solving

$$\dot{\sigma} = \frac{\partial \mathcal{H}_0}{\partial L} = 0, \dot{L} = -\frac{\partial \mathcal{H}_0}{\partial \sigma} = 0 \quad (4)$$

The linearized system is written as

$$\begin{bmatrix} d\ddot{\sigma} \\ d\ddot{L} \end{bmatrix} = \begin{bmatrix} \frac{\partial^2 \mathcal{H}_0}{\partial L \partial \sigma} & \frac{\partial^2 \mathcal{H}_0}{\partial L^2} \\ -\frac{\partial^2 \mathcal{H}_0}{\partial \sigma^2} & -\frac{\partial^2 \mathcal{H}_0}{\partial L \partial \sigma} \end{bmatrix} \begin{bmatrix} d\sigma \\ dL \end{bmatrix}$$

The EPs are obtained by solving

$$\begin{cases} d\ddot{\sigma} = 0 \\ d\ddot{L} = 0 \end{cases}$$

The linear stability of an EP can be determined from the

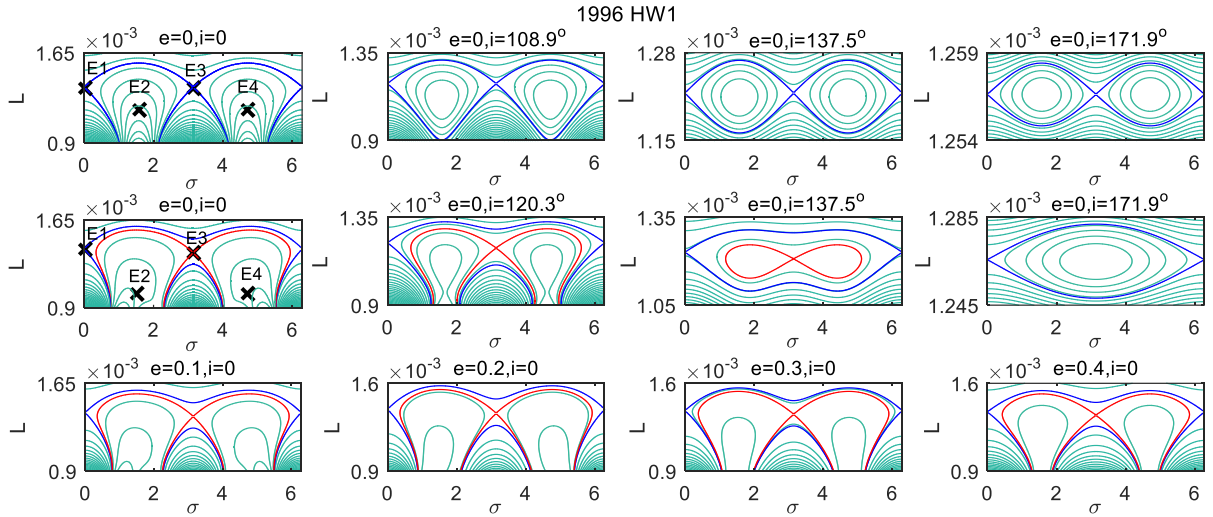


Fig. 1. The phase portrait of the Hamiltonian of 1996 HW1. Top row:  $\mathcal{H}_{0/2nd}$  for  $e = 0$ ,  $i = 0, 108.9^\circ, 137.5^\circ, 171.9^\circ$ ; middle row:  $\mathcal{H}_0$  for  $e = 0$ ,  $i = 0, 120.3^\circ, 137.5^\circ, 171.9^\circ$ ; bottom row:  $\mathcal{H}_0$  for  $i = 0$ ,  $e = 0.1, 0.2, 0.3, 0.4$ . The blue and red lines are the separatrix of the unstable EPs.

Jacobian matrix evaluated at the EP. The resonant frequency can be approximated at a stable EP  $(\sigma_s, L_s)$

as  $\sqrt{\frac{\partial^2 \mathcal{H}_0}{\partial L^2} \cdot \frac{\partial^2 \mathcal{H}_0}{\partial \sigma^2}} \Big|_{\sigma_s, L_s}$ . Taking the Hamiltonian value

corresponding to an unstable EP  $(\sigma_u, L_u)$ , denoted as  $\mathcal{H}_u$ , its level curve in the phase map is actually the separatrix that divides the motion into libration and circulation regions<sup>10</sup>. Along this curve,  $L$  passes through its maximum  $L_{max}$  and also minimum  $L_{min}$  at  $\sigma = \sigma_s$ . The resonance width is then calculated as  $\Delta L = L_{max} - L_{min}$  and is therefore only valid for the stable EPs.

### 3.2. Numerical Results

In this section, the EPs, their stability and the resonance width of asteroid 1996 HW1 are studied. This asteroid is selected since it is a good representative of highly bifurcated bodies. Its 4<sup>th</sup> degree and order spherical harmonics is given in Appendix B. It is noted here that all the angles except for inclination in this study are in radians. First, the dynamics due to the 2<sup>nd</sup> degree and order harmonics ( $C_{20}$  and  $C_{22}$ ) is studied, hereafter denoted as  $\mathcal{H}_{0/2nd}$ .

#### 3.3 1996 HW1

For 1996 HW1, the phase portrait of  $\mathcal{H}_{0/2nd}$  and  $\mathcal{H}_0$  is given in Fig.1. There are four unstable EPs appearing in the equatorial plane ( $i = 0$ ), which is consistent with our previous studies<sup>11</sup> and the results in Magri<sup>12</sup>. They are also marked out as E1, E2, E3 and E4. For small  $i$ , there is no region for libration and therefore all the EPs are unstable. It can be seen that the instability of the four EPs is already determined by the dynamics of  $\mathcal{H}_{0/2nd}$ . The inclusion of other harmonics however causes a strong distortion of the phase space. Two of the unstable EPs become stable at  $i \approx 108.9^\circ$  for  $\mathcal{H}_{0/2nd}$  and at  $i \approx 120.3^\circ$  for  $\mathcal{H}_0$ , indicating the destabilizing effects

of the highly irregular gravitational fields and the stability of the retrograde motion in this highly perturbed environment. Then the two EPs merge into one at  $i \approx 154.7^\circ$  also due to strong effects of  $C_{31}$  and finally disappear for the same reason: the effects of terms  $1 + c$  and  $s^2$ . The phase portrait is slightly influenced by  $e$  with the exception that an elongated orbit (with larger  $e$ ) is less influenced by the high degree and order harmonics, as shown in the bottom plots.

### 4. Second Resonance

For a qualitative study about the effect of the second degree of freedom on the 1:1 resonant dynamics,  $\mathcal{H}_1$  and  $\mathcal{H}_2$  should be considered. However, the inclusion of all terms in  $\mathcal{H}_1$  and  $\mathcal{H}_2$  is far from trivial. For this study, the dominant term of  $\mathcal{H}_2$  is taken into account. The dominant term, which has the largest amplitude, is given by

$$\mathcal{H}_{2d} = -\frac{\mu^4 R^2}{L^6} [F_{221} G_{212} (C_{22} \cos(2\sigma - 2g) + S_{22} \sin(2\sigma - 2g))] \quad (5)$$

In the current study, only  $\mathcal{H}_0$  and the dominant term  $\mathcal{H}_{2d}$

are taken into account and the resulting 2-DOF Hamiltonian is written as

$$\mathcal{H}_{2dof} = \mathcal{H}_0 + \mathcal{H}_{2d}$$

A new resonant angle  $2\sigma - 2g$  is introduced in the dynamics in addition to  $k\sigma$  ( $k = 1, 2, 3, 4$ ). A formal way to deal with this system is to treat  $\mathcal{H}_{2d}$  as a small perturbation to the integrable system  $\mathcal{H}_{2dof} = \mathcal{H}_0$ <sup>13</sup>). However, in our study, the perturbation of  $\mathcal{H}_{2d}$  is not limited to small values, due to the large variations of  $e$  and  $i$ . According to Chirikov<sup>14</sup>) and Morbidelli<sup>10</sup>), the dynamics of  $\mathcal{H}_{2dof}$  can be studied by observing the overlap process of nearby resonances using Poincaré maps. To a first approximation, each resonance is considered separately, only its own resonant angle is taken into account and the other one is neglected. The first resonance  $\mathcal{H}_{reson1}$  is actually  $\mathcal{H}_0$ , and the second resonance  $\mathcal{H}_{reson2}$  is defined as

$$\begin{aligned} \mathcal{H}_{reson2} &= -\frac{\mu^2}{2L^2} - \dot{\theta}L - \frac{\mu^4 R^2}{L^6} F_{201} G_{210} C_{20} + \mathcal{H}_{2d} \\ &= -\frac{\mu^2}{2L^2} - \dot{\theta}L - \frac{\mu^4 R^2}{L^6} (1-e^2)^{\left(\frac{-3}{2}\right)} \left( -\frac{1}{2} + \frac{3s^2}{4} \right) C_{20} \\ &\quad - \frac{\mu^4 R^2}{L^6} \frac{3}{2} \left( \frac{9e^2}{4} + \frac{7e^4}{4} \right) s^2 \left[ C_{22} \cos(2\sigma - 2g) \right. \\ &\quad \left. + S_{22} \sin(2\sigma - 2g) \right] \end{aligned} \quad (6)$$

which only includes one resonant angle  $2\sigma - 2g$ . Its location needs to be solved first and then the Poincaré maps of the single-resonance dynamics are computed respectively on the same section in the vicinity of their location. If  $\mathcal{H}_{2d}$  is small enough, the separatrix of  $\mathcal{H}_{reson2}$  is further away from that of  $\mathcal{H}_{reson1}$  and the two resonances are slightly influenced by each other. Tiny chaotic layers are probably generated around the separatrix. Otherwise, if  $\mathcal{H}_{2d}$  is large, the separatrix of the two resonances intersect, their dynamical domains overlap, and each resonance is significantly affected by the other one.

The chaotic layers extend to large-region chaos that dominates the phase space. Since  $\mathcal{H}_{reson1}$  is the dominant dynamics of our 1:1 resonant model, the focus is put on how  $\mathcal{H}_{reson1}$  is influenced by  $\mathcal{H}_{reson2}$ , which can also be interpreted as how much the 1-DOF dynamics is affected by a perturbation.

#### 4.1 The Location and Width of $\mathcal{H}_{reson2}$

The location and width of  $\mathcal{H}_{reson1}$  have been obtained in Section 3. Since we want to apply Poincaré sections to study the dynamics, the section of the map is first defined here as  $g = \pi/2, \dot{g} > 0$  in the  $L - \sigma$  plane. Since  $\mathcal{H}_{reson1}$  has 1-DOF, its Poincaré map is the same with its phase portrait in the phase space. The location of  $\mathcal{H}_{reson2}$  in this section can be obtained by numerically solving

$$\begin{cases} 2\dot{\sigma} - 2\dot{g} = \frac{2\partial\mathcal{H}_{reson2}}{\partial L} - \frac{2\partial\mathcal{H}_{reson2}}{\partial G} = 0 \\ \mathcal{H}_{reson2}(\sigma_0, g_0, L^*, G^*) = \mathcal{H}_{separatrix} \end{cases} \quad (7)$$

in which  $\sigma_0 = g_0 = \pi/2$ .  $\mathcal{H}_{separatrix}$  is the Hamiltonian value of the separatrix of  $\mathcal{H}_{reson1}$  which is also the energy constant of the section.  $L^*$  and  $G^*$  represent the variables that need to be solved. As  $\mathcal{H}_{reson2}$  itself is a 2-DOF system, the pendulum model cannot be applied for approximating its resonance width. Therefore, based on the dynamical properties of the Poincaré map, a full numerical estimation is used. By integrating from the initial point  $(\sigma_0, g_0, L^*, G^*)$  for moderate iterations, a curve is obtained which is either the upper or the lower part of the separatrix of  $\mathcal{H}_{reson2}$  on the section. If it is the upper part,  $L_{max}$  is directly obtained by taking record of the maximum point of the curve.  $L_{min}$  is the minimum of the lower border obtained by integrating from the point  $(\sigma_0, g_0, L^* - \delta L, G)$  with  $\delta L$  depending on the dynamics studied and vice versa. The curves acquired are the separatrix of  $\mathcal{H}_{reson2}$ . Therefore, the width of  $\mathcal{H}_{reson2}$  is approximated by  $L_{max} - L_{min}$ , which is already good enough for the current study.

Given that the maxima and minima of  $\mathcal{H}_{reson1}$  and  $\mathcal{H}_{reson2}$  are denoted as  $L_{max1}, L_{min1}$  and  $L_{max2}, L_{min2}$ , respectively, the relative locations of the two resonances can be characterized by  $L_{min1} - L_{max2}$  and  $L_{min1} - L_{min2}$ . The former one, which is the distance between the lower borders

( $126^\circ \lesssim i < 180^\circ$ ) of libration motion of  $\mathcal{H}_{reson1}$  (shown in Fig.3), its second degree of freedom dynamics is studied first. In Fig.2, the upper plots give the separatrices of the two

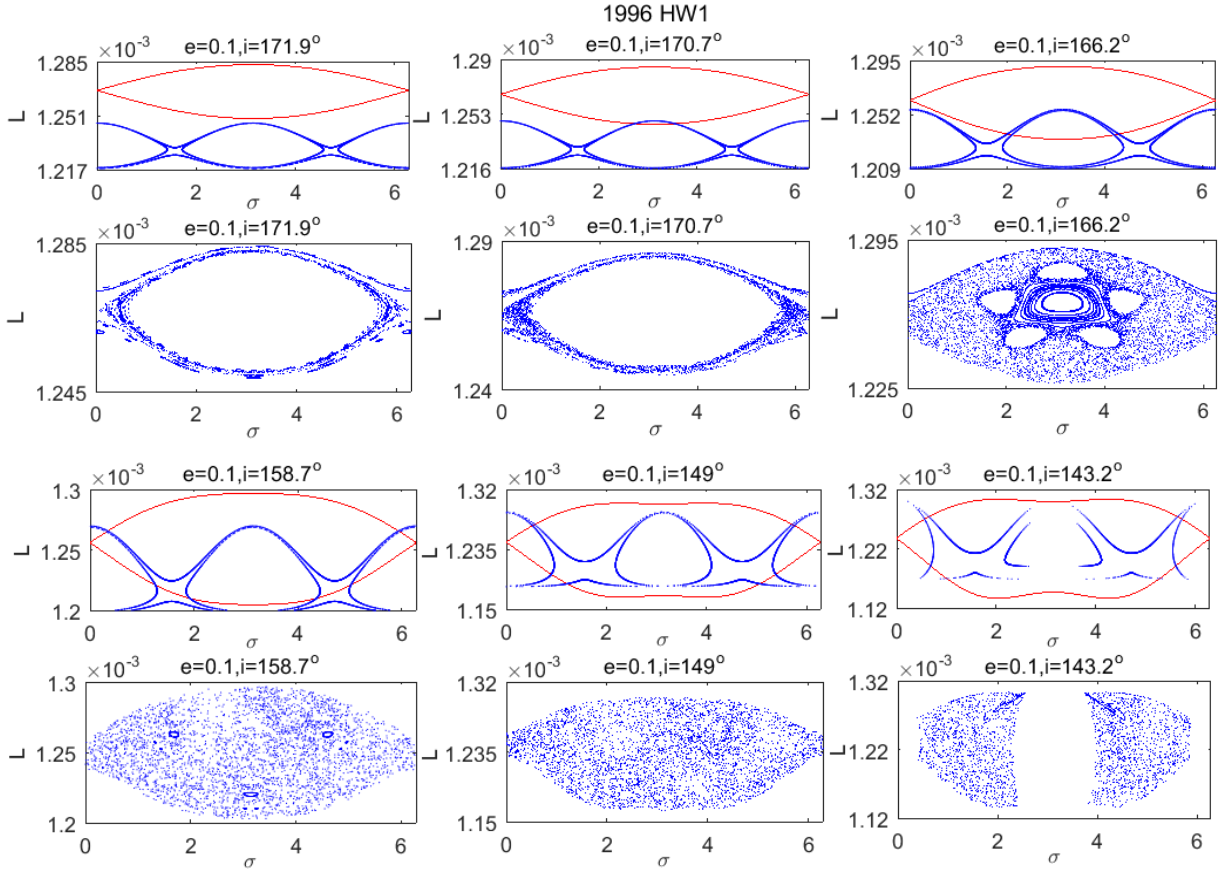


Fig. 2. First and third rows: the separatrices of resonances  $\mathcal{H}_{reson1}$  (red) and  $\mathcal{H}_{reson2}$  (blue) on the section  $g = \pi/2, \dot{g} > 0$ ; second and fourth rows: the phase space of the corresponding  $\mathcal{H}_{2dof}$ ; both for  $e = 0.1, i = 171.9^\circ, 170.7^\circ, 166.2^\circ, 158.7^\circ, 149^\circ$  and  $143.2^\circ$ .

of the two resonances, is positive if the two resonances are totally separated and becomes negative as the resonances start to overlap each other. The latter one is actually the measurement of the extent of overlap of the two resonances. Its non-positive value indicates that one resonance is completely within the other one. For different combinations of  $e$  and  $i$ , the 2-DOF Hamiltonian  $\mathcal{H}_{2dof}$  is studied for 1996 HW1, Vesta and Betulia.

#### 4.2 The effect of $i$

Since 1996 HW1 only has a limited inclination range

resonances in the Poincaré maps, which are the boundaries of their phase space. The bottom plots are the phase space of  $\mathcal{H}_{2dof}$  on the same section, both for  $i$  changing from  $171.9^\circ$  to  $143.2^\circ$  at the example  $e = 0.1$ . Fig.2 reflects the relationship of the distance between the two resonances  $\mathcal{H}_{reson1}$  and  $\mathcal{H}_{reson2}$  and the extent of chaotic region of  $\mathcal{H}_{2dof}$ .

For  $i = 171.9^\circ$ , even though the resonances do not overlap (but are close), tiny chaotic layers appear in the vicinity of the separatrix of  $\mathcal{H}_{2dof}$ . When there is a small overlap at  $i = 166.2^\circ$ , the chaotic layer is extended but a large libration region still remains. With the increase of the overlap from  $i = 166.2^\circ$ , a large part of the phase space is occupied by chaos. The regular region shrinks to a limited area at the center of the phase space and meanwhile five islands appear around it,

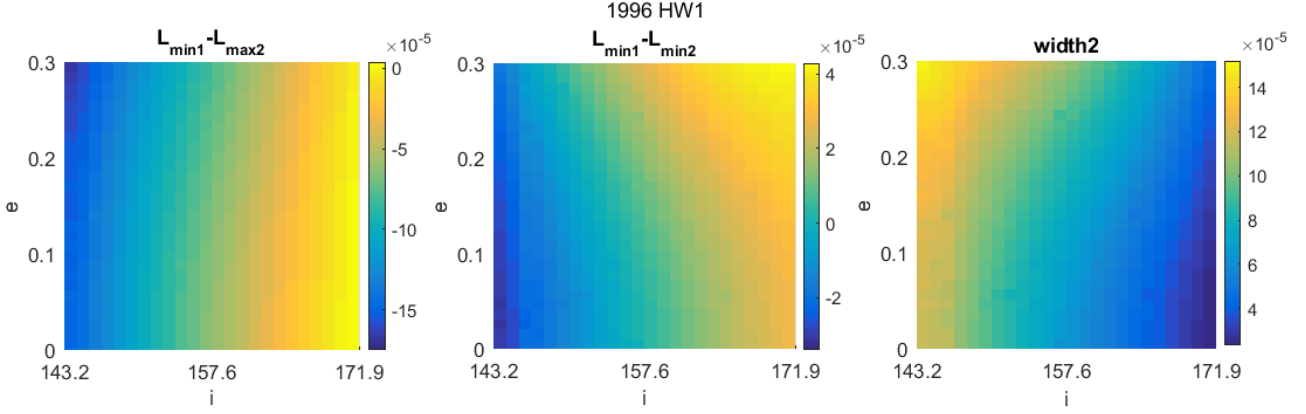


Fig. 3. The distance between  $\mathcal{H}_{reson1}$  and  $\mathcal{H}_{reson2}$  measured as  $L_{min1} - L_{max2}$  (left) and  $L_{min1} - L_{min2}$  (middle), and the width of  $\mathcal{H}_{reson2}$  (right).

which is due to the high-order resonances between  $\mathcal{H}_{reson1}$  and  $\mathcal{H}_{reson2}$ . With the further decrease of  $i$  to  $158.7^\circ$ ,  $\mathcal{H}_{reson2}$  is almost completely inside  $\mathcal{H}_{reson1}$  and there are only three small KAM tori left, indicating the system is transiting to global chaos. In addition, the original stable EP becomes unstable as the center part is already chaotic. Although the dynamics is completely chaotic at  $i = 149^\circ$ , the chaos is still bounded by the separatrix of  $\mathcal{H}_{reson1}$ . However, finally at  $i = 143.2^\circ$  the whole structure of  $\mathcal{H}_{reson1}$  can not be kept and the continuity of the phase space is broken. It is noticed that this break is consistent with the break of the separatrix of  $\mathcal{H}_{reson2}$  at the same range of  $\sigma$ , implying a

produces no crossings on the section which is defined as  $\dot{g} > 0$ . This phenomenon will be discussed in detail in the next section.

In summary,  $i$  has a great influence on the 2-DOF dynamics at constant  $e$ . When  $i$  decreases,  $\mathcal{H}_{reson2}$  is strengthened as it includes the term  $s^2$  (as seen in Eq.(6)) and its resonance width increases. However, its location does not deviate much. For  $\mathcal{H}_{reson1}$ , not only its width is increasing but also its location is moving downward. Ultimately, the two resonances totally overlap and have a strong interaction with each other. Nevertheless, the width of  $\mathcal{H}_{2dof}$  is determined by  $\mathcal{H}_{reson1}$ , which is seen from both  $L$  values, although the inner structure of the phase space has been totally affected.

### 4.3. The Effect of $e$

To study the effect of  $e$  on the dynamics, the contour map

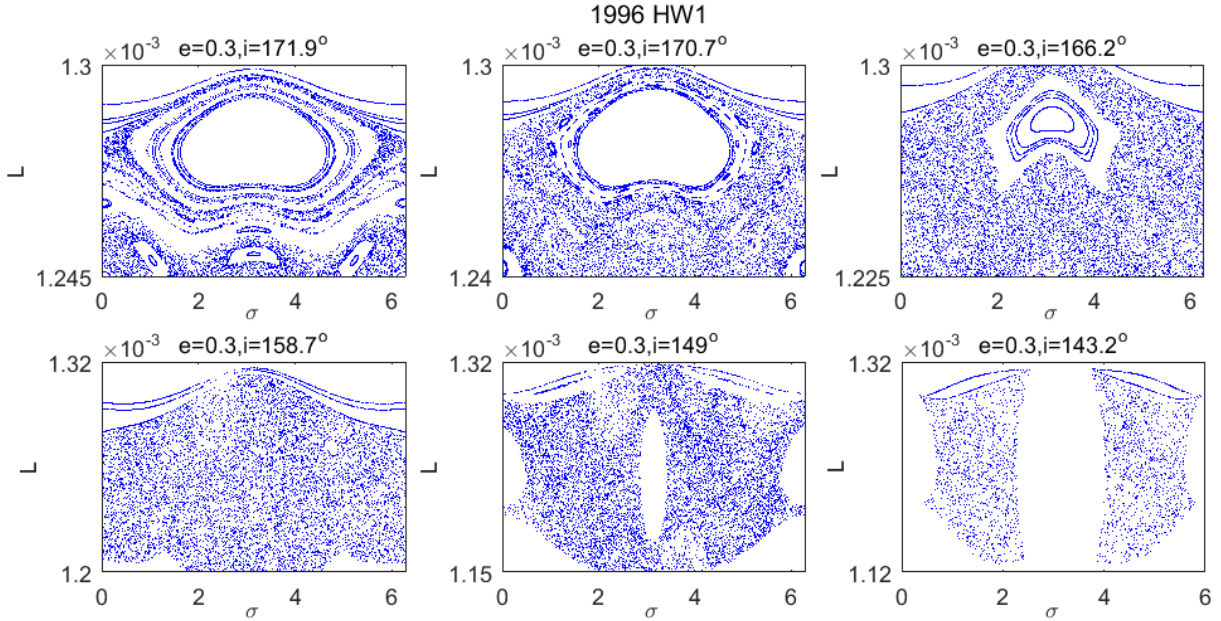


Fig. 4. The phase space of  $\mathcal{H}_{2dof}$  at  $e = 0.3$  for  $i = 171.9^\circ, 170.7^\circ, 166.2^\circ, 158.7^\circ, 149^\circ, 143.2^\circ$ .

significant perturbation of  $\mathcal{H}_{reson2}$  on the total dynamics. The break of  $\mathcal{H}_{reson2}$ 's separatrix attributes to the fact that the time derivative of  $g$  ( $\dot{g}$ ) changes sign from positive to negative after  $i$  crossing some specific value, and therefore it

of the distance of the two resonances and also the width of the second resonance are given in the  $e - i$  plane in Fig.6. In the left plot, the yellow region indicates the situation of non-overlap and slight overlap. In the middle plot, the green and blue areas demonstrate the situation when  $\mathcal{H}_{reson2}$  moves totally inside  $\mathcal{H}_{reson1}$  and the overlap between the two is complete. The right plot demonstrates that the width of  $\mathcal{H}_{reson2}$  is also enlarged when  $e$  becomes large, which can

be proven to be caused by the term  $(9e^2/4 + 7e^4/4)$  in  $\mathcal{H}_{reson2}$ . Therefore, the largest distance of  $\mathcal{H}_{reson1}$  and  $\mathcal{H}_{reson2}$  is witnessed at the down-right corner and  $\mathcal{H}_{reson2}$  approaches its highest location at the upper-left corner in the left plot. In addition, as  $e$  increases and  $i$  decreases,  $\mathcal{H}_{reson2}$  becomes stronger (as indicated by the resonance width) and has a significant influence on the dynamics of  $\mathcal{H}_{reson1}$ .

Therefore, given a specific  $e$  and  $i$ , an estimate from this contour map can be made on when small chaotic layers appear and when large chaotic seas are expected. As an example, for  $e = 0.1$ , tiny chaotic layers are apparent at  $i = 171.9^\circ$  when the two resonances start to overlap; the last KAM tori disappear and the phase space is full with chaos around  $i = 158.2^\circ$ .

For a more complete understanding, the phase space of  $\mathcal{H}_{2dof}$  at  $e = 0.3$  with different  $i$  is given in Fig. 4. Compared to Fig.5, the upper plots of Fig.7 show that the large  $e$  distorts the main island, which originally has a circular or ellipsoidal shape. The chaos is more abundant and the size of the main island reduces and a new phase structure is generated at the bottom of the plot, due to the stronger influence of  $\mathcal{H}_{reson2}$ . In addition, the lower half of the chaos is thicker than the upper part, as it is more influenced by the perturbation from  $\mathcal{H}_{reson2}$  which approaches  $\mathcal{H}_{reson1}$  from the bottom direction. In addition, the islands appearing at the bottom area of the phase space can be explained by the direct interaction of  $\mathcal{H}_{reson1}$  and  $\mathcal{H}_{reson2}$  in that region. Furthermore, the lower three plots are full of chaos.

#### 4.4 Maximal Lyapunov Characteristic Exponent of Chaotic Orbits

In addition to the above study about the extent of chaotic layers, the chaos can also be characterized quantitatively by calculating the value of the maximal Lyapunov Characteristic Exponent (mLCE), which is an indicator of the regular or chaotic properties of orbits<sup>15)</sup>. Its basic idea is to measure the distance between two orbits that start close, until infinite time  $t \rightarrow \infty$ . It characterizes the average growth rate of a small perturbation of the solution of a dynamical system and is defined as

$$\lambda = \lim_{t \rightarrow \infty} \frac{1}{t} \sum_0^t \ln \|\mathbf{v}(t)\|$$

in which  $\mathbf{v}(t)$  is the deviation vector with respect to the reference orbit at time  $t$ . It is also the solution of the corresponding variational equations of the dynamical system. If  $\lambda > 0$ , the orbit is chaotic; if  $\lambda = 0$ , the orbit is regular. The numerical algorithm applied here is the standard method originally developed by Benettin and Galgani<sup>16)</sup>. Its detailed implementation can be found in Skokos<sup>15)</sup>. It has to be mentioned that for regular orbits it might take a long time for  $\lambda$  to achieve zero. However, within a moderate time interval the tendency to zero is already visible.

Since it is obvious that large  $e$  introduces stronger chaos, the mLCE of orbits selected from the chaotic and regular regions (if there is no chaos) on the maps from Fig. 2 are

given in Fig. 5. These maps primarily indicate the effect of  $i$  on dynamics at  $e = 0.1$ . The integration time is chosen such that a stable value of all the mLCE values can be achieved.

It can be seen that the more inclined the orbit, the larger mLCE value it has, indicating a stronger tendency to chaos. The resonant orbits around 1996 HW1 have large mLCE values (magnitude  $10^{-5}$ ), due to its highly irregular gravitational field. Additionally, the mLCE values not only can identify the chaotic behavior of orbits, but also give us a hint on the extent of chaotic property.

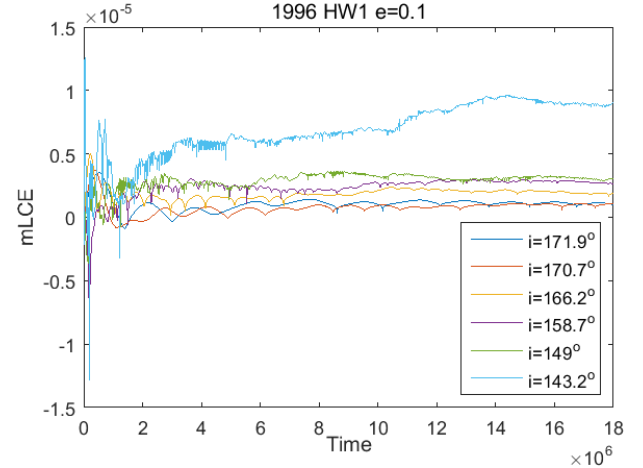


Fig. 5. The mLCE of regular and chaotic orbits from the Poincaré maps of  $\mathcal{H}_{2dof}$  for 1996 HW1.

#### 5. Conclusion

In this study, a 2-DOF Hamiltonian of the 1:1 resonant dynamics of a gravitational field up to degree and order 4 was built. The 1-DOF Hamiltonian  $\mathcal{H}_0$  was first studied by finding the EPs and examining their stability for non-circular and non-polar orbits around 1996 HW1. This  $\mathcal{H}_0$  was proven to capture the main characteristics of the 1:1 resonant dynamics. For  $\mathcal{H}_0$ ,  $i$  was found to play a significant role on the number of EPs. When  $i$  approaches  $\pi$ , there is only one stable EP left, due to the dominant strength of  $C_{31}$  over  $C_{22}$  on the structure of the phase space. The 2<sup>nd</sup> degree and order harmonics largely determine the stability of the EP, while the higher order terms either introduce new EPs and change the resonance width or break the symmetry of the dynamics.

By applying Poincaré maps, the 2-DOF Hamiltonian  $\mathcal{H}_{2dof}$  was then investigated. Two Hamiltonians  $\mathcal{H}_{reson1}$  and  $\mathcal{H}_{reson2}$  were defined in this 2-DOF model and their locations and widths were determined numerically for different combinations of  $e$  and  $i$ .

With the overlap criteria, the extent of chaotic regions was qualitatively explained by the distance between the two resonances as well as their resonance strength. For small  $e$  and  $i$  close to  $180^\circ$ , the dynamics of  $\mathcal{H}_{reson1}$  around the stable EP is hardly influenced for the situation when  $\mathcal{H}_{reson1}$  and  $\mathcal{H}_{reson2}$  are further apart. When  $i$  gets further away from the equatorial plane,  $\mathcal{H}_{reson2}$  becomes close to and almost interacts with  $\mathcal{H}_{reson1}$ . When the two resonances have an obvious overlap for  $i$  getting close to the polar region, large chaos becomes apparent and new islands come forth in the phase space. Though the structure of the phase

space is largely determined by  $i$ , a large value of  $e$  definitely gives rise to strong perturbations of  $\mathcal{H}_{reson2}$ , which makes the main island distorted and the chaotic region extended. In addition, the mLCEs of the chaotic and regular orbits were calculated, from which the above conclusion was proven quantitatively.

The results and analyses in this paper serve as an example of the relationship among resonance overlap, extent of chaos and strength of the perturbing terms. The 2-DOF resonant dynamics of other main motion resonances, e.g. 1:2, 2:3, 3:2, can also be investigated with the approach applied in this paper.

## Acknowledgments

X. Hou also thanks the support from the National Science Foundation of China Grant (11322330).

## Appendix A

Table A1 The primary zonal and tesseral terms contributing to the 1:1 resonance.

$n$	2	2	3	3	4	4	4
$m$	0	2	1	3	0	2	4
$p$	1	0	1	0	2	1	0
$q$	0	0	0	0	0	0	0
$\Theta_{nmpq}$	0	$2\sigma$	$\sigma$	$3\sigma$	0	$2\sigma$	$4\sigma$

The expressions of  $\mathcal{H}_1$  and  $\mathcal{H}_2$  are given as

$$\begin{aligned} \mathcal{H}_1 = & -\frac{\mu^4 R^2}{L^6} \left[ F_{210} G_{20-1} (C_{21} \cos(\sigma + g) + S_{21} \sin(\sigma + g)) \right. \\ & \left. + F_{211} G_{211} (C_{21} \cos(\sigma - g) + S_{21} \sin(\sigma - g)) \right] \\ & -\frac{\mu^5 R^3}{L^8} \left[ F_{301} G_{31-1} (C_{30} \cos g + S_{30} \sin g) \right. \\ & \left. + F_{302} G_{321} (C_{30} \cos g - S_{30} \sin g) \right] \\ & -\frac{\mu^6 R^4}{L^8} [F_{411} G_{41-1} (C_{41} \cos(\sigma + g) + S_{41} \sin(\sigma + g)) + \\ & F_{412} G_{421} (C_{41} \cos(\sigma - g) + S_{41} \sin(\sigma - g)) \\ & + F_{430} G_{40-1} (C_{43} \cos(3\sigma + g) + S_{43} \sin(3\sigma + g)) \\ & + F_{431} G_{411} (C_{43} \cos(3\sigma - g) + S_{43} \sin(3\sigma - g))] \end{aligned} \quad (A.1)$$

$$\begin{aligned} \mathcal{H}_2 = & -\frac{\mu^4 R^2}{L^6} [F_{221} G_{212} (C_{22} \cos(2\sigma - 2g) + S_{22} \sin(2\sigma - 2g))] \\ & -\frac{\mu^5 R^3}{L^8} \left[ F_{310} G_{30-2} (C_{31} \cos(\sigma + 2g) + S_{31} \sin(\sigma + 2g)) \right. \\ & \left. + F_{312} G_{322} (C_{31} \cos(\sigma - 2g) + S_{31} \sin(\sigma - 2g)) \right. \\ & \left. + F_{331} G_{312} (C_{33} \cos(3\sigma - 2g) + S_{33} \sin(3\sigma - 2g)) \right] \\ & -\frac{\mu^6 R^4}{L^8} [F_{401} G_{41-2} (C_{40} \cos(2g) + S_{40} \sin(2g)) + \\ & F_{422} G_{422} (C_{42} \cos(2\sigma - 2g) + S_{42} \sin(2\sigma - 2g))] \end{aligned}$$

(A.2)

## Appendix B

Table B1 The 4<sup>th</sup> degree and order spherical harmonics of 1996 HW1.

1996 HW1 (all $S_{nm}$ terms are zero)					
$C_{20}$	$-1.21847 \times 10^{-1}$	$C_{31}$	$-1.3964 \times 10^{-2}$	$C_{41}$	0
$C_{21}$	0	$C_{32}$	0	$C_{42}$	$-4.258 \times 10^{-3}$
$C_{22}$	$5.8547 \times 10^{-2}$	$C_{33}$	$2.547 \times 10^{-3}$	$C_{43}$	0
$C_{30}$	0	$C_{40}$	$3.8779 \times 10^{-2}$	$C_{44}$	$5.16 \times 10^{-4}$

## References

- 1) Delhaise, F., and Henrard, J.: The problem of critical inclination combined with a resonance in mean motion in artificial satellite theory. *Celest. Mech. Dyn. Astron.*, **55**(1993), pp. 261–280.
- 2) Scheeres, D.: Dynamics about uniformly rotating triaxial ellipsoids: applications to asteroids. *Icarus*, **110**(1994), pp. 225–238.
- 3) Scheeres, D., Ostro, S., Hudson, R., Werner, R.: Orbits close to asteroid 4769 Castalia. *Icarus*, **121**(1996), pp. 67–87.
- 4) Hu, W., and Scheeres, D.: Numerical determination of stability regions for orbital motion in uniformly rotating second degree and order gravity fields. *Planet. Space Sci.*, **52**(2004), pp. 685–692.
- 5) Olsen, Ø.: Orbital resonance widths in a uniformly rotating second degree and order gravity field. *Astron. Astrophys.* **449**(2006), pp. 821–826.
- 6) Delsate, N.: Analytical and numerical study of the ground-track resonances of Dawn orbiting Vesta. *Planet. Space Sci.*, **59**(2011), pp. 1372–1383.
- 7) Tzirti, S., and Varvoglis, H.: Motion of an Artificial Satellite around an Asymmetric, Rotating Celestial Body: Applications to the Solar System. PhD dissertation, Aristotle University of Thessaloniki, Greece, 2014.
- 8) Compère, A., Lemaître, A., and Delsate, N.: Detection by MEGNO of the gravitational resonances between a rotating ellipsoid and a point mass satellite. *Celest. Mech. Dyn. Astron.*, **112**(2012), pp. 75–98.
- 9) Kaula, W.M.: Theory of satellite geodesy: applications of satellites to geodesy, Blaisdell Publishing Company, Massachusetts, 1966.
- 10) Morbidelli, A.: Modern celestial mechanics: aspects of solar system dynamics. Taylor & Francis, London, 2002.
- 11) Feng, J., Noomen, R., and Yuan, J.: Orbital Motion in the Vicinity of the Non-collinear Equilibrium Points of a Contact Binary Asteroid. *Planet. Space Sci.*, **117**(2015), pp. 1–14.
- 12) Magri, C., Howell, E. S., Nolan, M. C., et al., Radar and photometric observations and shape modeling of contact binary near-Earth asteroid (8567) 1996 HW1. *Icarus*, **214**(2011), pp. 210–227.
- 13) Henrard, J.: A semi-numerical perturbation method for separable Hamiltonian systems. *Celest. Mech. Dyn. Astron.*, **49**(1990), pp. 43–67.
- 14) Chirikov, B.V.: A universal instability of many-dimensional oscillator systems. *Phys. Rep.*, **52**(1979), pp. 263–379.
- 15) Skokos, C.: The Lyapunov characteristic exponents and their computation. Dynamics of small solar system bodies and exoplanets, Springer, Berlin, 2010.
- 16) Benettin, G., and Galgani, L.: Lyapunov characteristic exponents and stochasticity. Cargese, 1979.